FABRICATION AND PETROPHYSICAL CHARACTERIZATION OF ARTIFICIAL CARBONATE ROCKS WITH MULTISCALE POROSITY SINTERED IN A CO_2 ATMOSPHERE

Mateus Mota Morais[a*] - mateus.morais@usp.br – ORCID 0000-0002-5318-8129
Everton Lucas-Oliveira[b] – everton.lucas.oliveira@usp.br – ORCID 0000-0003-1353-918X
Tito José Bonagamba[b] – tito@ifsc.usp.br – ORCID 0000-0001-8894-9170
Pedro Tupã Pandava Aum[c,d] – pedroaum@ufpa.br – ORCID 0000-0002-2339-9865
Cláudio Regis dos Santos Lucas[c] – claudiolucas@ufpa.br – ORCID 0000-0001-5443-462X
Daniel Nobre Nunes da Silva[c] – danielnobre@ufpa.br – ORCID 0000-0002-0949-6060
Carlos Alberto Fortulan[a] – fortulan@usp.br – ORCID 0000-0002-2259-9910

[a]Department of Mechanical Engineering, São Carlos School of Engineering, University of São Paulo, Trabalhador São-carlense, 400, São Carlos 13566-590, Brazil
[b]São Carlos Institute of Physics, University of São Paulo, PO Box 369, 13560-970, São Carlos, SP, Brazil
[c]Faculty of Petroleum Engineering, Federal University of Pará, Salinópolis, Brazil
[d]Pos-graduation of Chemical Engineering PPGEQ-ITEC-UFPA, Federal University of Pará, Belém, Brazil

[*]Corresponding author at: Department of Mechanical Engineering, São Carlos School of Engineering, University of São Paulo, Trabalhador São-carlense, 400, São Carlos, 13566-590, Brazil.
E-mail: mateus.morais@usp.br

Accepted manuscript published at Geoenergy Science and Engineering
DOI: https://doi.org/10.1016/j.geoen.2023.212096

ABSTRACT

Carbonate rock samples are used in research related to enhanced oil recovery, acid stimulation, calibration of well-logging tools, and validation of numerical petrophysical simulations. However, natural carbonates samples are extremely heterogeneous and have limited availability, compromising experimental analyses. Furthermore, the previous attempts to fabricate synthetic rock replicas were unable to produce samples with pure calcium carbonate composition and multiscale porosity. This paper presents the fabrication of artificial rock with pure calcite composition. Calcite powder was compacted with a pore former (ammonium bicarbonate) and sintered at 850°C with CO_2 atmosphere to avoid the decomposition of the $CaCO_3$. Five groups of samples were produced: partially sintered, sintered with 5, 10, and 20% of the large porogen, and with 20% of the small porogen. The artificial rocks were characterized through X-ray diffraction, porosimetry, X-ray microtomography, scanning electron microscopy, mercury injection, permeability, nuclear magnetic resonance, mechanical compression, and acidizing core flooding experiments. The results revealed that the artificial rocks have a controlled bimodal porosity, with large pores induced by the pore formers (83 - 211 µm) and nanometric intrinsic pores and fractures. In addition, the samples presented a high mechanical resistance (40 to 126 MPa), similar to natural rocks, and could withstand water immersion and even the core flooding tests. The main drawback was the low permeability (0.05-0.06 mD) achieved, an aspect to be improved in future works. The reported methodology is a significant advance because it allows independently tuning the porosity and pore size distribution, controlling the resultant petrophysical properties in a reproducible way without compromising the chemical constitution, enabling several applications in research.

Keywords: Calcite; Carbonate rocks; Synthetic rocks; Porosity; Core plug; Sintering.

Abbreviations: X-ray diffraction (XRD), Microcomputed tomography (µCT), Nuclear Magnetic Resonance (NMR)

1. INTRODUCTION

Carbonate rocks, which comprise about half of the world's petroleum reservoirs, are mainly composed of carbonate sediments (calcite, aragonite, and dolomite) (Alyafei, 2021; Baker et al., 2015a; R. C. Selley, 2005; R C Selley, 2005; Speight, 2017; Tucker and Wright, 1990). Their pore structure is known to be very heterogeneous due to the complex chemical and physical processes during rock formation and diageneses (Baker et al., 2015a; Machel, 2005; Speight, 2017; Tucker and Wright, 1990). For instance, the porosity of limestones and dolomites can usually vary from 5 to 30% (Baker et al., 2015a; Speight, 2017; Tucker and Wright, 1990), with some of them reaching up to 52% (Wu et al., 2020), with pore sizes ranging from nanopores (<1 μm) up to caverns (> 1 m) (Choquette and Pray, 1970; Loucks et al., 2012; Tucker and Wright, 1990). Carbonate core plugs usually present this multiscale porosity, with some regions very dense, others with large macropores, and others with a variable amount of microporosity (Ji et al., 2015, 2012). Moreover, the volume and connectivity of these regions have important effects on the mechanical properties and the permeability of carbonate rocks (Ji et al., 2015, 2012; Speight, 2017; Wang et al., 2017, 2015). As a result, their permeability can be lower than 1 mD but reach up to 10,000 mD if fractures and vuggy pores are interconnected (Baker et al., 2015a; Speight, 2017; Tucker and Wright, 1990). Furthermore, carbonates commonly present an anisotropic permeability because of fractures (Baker et al., 2015a; Ganat, 2020), dissolution features (such as stylolites (Heap et al., 2018)), and the changes in the connectivity of heterogeneous multimodal pore structures caused by hydromechanical loadings (Dautriat et al., 2011).

Because of their importance in the oil and gas industry, carbonate rock core plugs have many applications. For example, they are used for characterizing the petrophysical properties of reservoirs (Alyafei, 2021; Baker et al., 2015b; Darling, 2005), developing and validating numerical models and simulations, obtaining experimental correlations between the microstructure and the petrophysical and mechanical properties and rock-fluid interactions (Carbillet et al., 2022, 2021; Chang et al., 2006; Ishutov et al., 2018b; Kong et al., 2021a; Lézin et al., 2009; Wang et al., 2015), calibrating well-logging and characterization tools (Fedrizzi et al., 2018; Kong et al., 2021a), and performing core flooding experiments in enhanced oil recovery and acid stimulation studies (Baker et al.,

2015b; de Castro Dantas et al., 2020; Fedrizzi et al., 2018; Lucas et al., 2020; Wang et al., 2017; Zakaria et al., 2015).

However, using natural rocks in experiments has some drawbacks: First, they are usually limited in number and can have a high cost of extraction (Almetwally and Jabbari, 2020; Florez et al., 2019; Florez and Ferrari, 2021). This limitation is critical for experiments that require several samples, especially destructive tests such as mercury injection porosimetry, core flooding, and compressive tests (Almetwally and Jabbari, 2020; Ishutov et al., 2018a; Kong et al., 2019b, 2019a). Second, because natural carbonate rocks are remarkably heterogeneous, there is large sample variability, even within samples drilled from the same rock. This natural heterogeneity between samples introduces experimental uncertainty, making it difficult to obtain comparable and reproducible results (Almetwally and Jabbari, 2020; de Castro Dantas et al., 2020; Fu et al., 2020; Gell et al., 2019; Head and Vanorio, 2016; Kong et al., 2019b, 2019a; Zakaria et al., 2015). It is also hard to obtain strong correlations between petrophysical structure and properties (Chang et al., 2006; Lézin et al., 2009). Finally, it is challenging to obtain natural rocks with predetermined characteristics intended for validation tests, such as a predetermined porosity and grain size distribution (Carbillet et al., 2022, 2021) or a fracture with a determined shape or aspect ratio (Gell et al., 2019), or a specific chemical composition or wettability (Ferrari et al., 2021; Kushnir et al., 2015).

As an alternative, some authors have proposed producing artificial rocks with petrophysical and chemical properties similar to natural carbonates (Cardoso et al., 2018; de Melo, 2012; D'Eurydice et al., 2016; El Husseiny and Vanorio, 2015; Fedrizzi et al., 2018; Florez et al., 2019; Florez and Ferrari, 2021; Ishutov et al., 2018b; Kong et al., 2021a; Kushnir et al., 2015; Piane, Delle et al., 2015; Wang et al., 2017, 2015). Their goal is to produce tailored rock replicas with controllable and reproducible features, allowing the systematic variation of the mineralogical and geometrical characteristics and the consequent petrophysical properties. Additionally, rock replicas can be produced at a lower cost than the extraction of natural samples (Fedrizzi et al., 2018), allowing a larger number of specimens for experiments.

Nevertheless, mimicking both the chemical composition and the microstructure of natural carbonate rocks is no easy task. The first challenge is consolidating carbonate without decomposition or contamination. The manufacturing of ceramic materials commonly includes a sintering stage at high temperatures, which promotes the coalescence of the material particles resulting in volumetric shrinkage, porosity reduction,

and increased mechanical resistance (Reed, 1995; Richerson and Lee, 2018). For instance, the sintering of glass beads has been applied to produce artificial rocks with controlled porosity and grain size distribution for compaction mechanics studies (Carbillet et al., 2022, 2021). However, calcium carbonate starts to thermally decompose into calcium oxide and carbon dioxide above 550°C (Criado et al., 1995; Escardino et al., 2013; Viswanathan et al., 2010), below the required sintering temperature, which makes it a complex process to be applied to fabricate carbonate rocks. In fact, most previous studies were only able to produce calcium carbonate artificial rocks with the aid of some type of glue, cement, or other binder materials (El Husseiny and Vanorio, 2015; Fahim Salek et al., 2022; Fedrizzi et al., 2018; Florez et al., 2019; Florez and Ferrari, 2021; Piane, Delle et al., 2015; Wang et al., 2017, 2015), or employing hot isostatic pressure with an inert gas (Kushnir et al., 2015). Despite that, many artificial rocks in literature have low mechanical resistance and do not withstand immersion and core flooding experiments. Furthermore, the materials added may affect the wettability and chemical properties, compromising investigations where the rock-fluid interactions and the matrix reactivity are essential.

The second challenge is reproducing the heterogeneous multiscale porosity of carbonates. The reported artificial carbonate rocks usually present only homogeneous nano and microporosity (<10 µm) and low permeability (El Husseiny and Vanorio, 2015; Fedrizzi et al., 2018; Florez et al., 2019; Florez and Ferrari, 2021) with very few succeeding in producing large pores and fractures with the aid of other materials besides carbonate (Cardoso et al., 2018; Lucas-Oliveira et al., 2018; Wang et al., 2017). On the other hand, 3D printing, an emerging and promising alternative, can reproduce the large pores of carbonates but is limited by the minimum resolution of conventional 3D printers (≈25-300 µm) and the lack of commercial materials to mimic the rock mineralogy (Gibson et al., 2015; Ishutov, 2019; Ishutov et al., 2018b, 2018a; Kong, 2019; Kong et al., 2021b, 2021a). Recently, a few papers described 3D printing of calcium carbonate parts, which can open up new opportunities in a near future for the development of artificial rocks (Albalawi et al., 2021; Elsayed et al., 2020; Morais et al., 2023; Sauerwein and Doubrovski, 2018; Shaked et al., 2021).

This paper presents a fabrication method to produce artificial carbonate rocks with multiscale porosity and pure calcite composition that overcome many limitations of the reported alternatives. The process comprises isostatically compacting the carbonate powder with fugitive pore formers (ammonium bicarbonate) to tune the vuggy porosity

and sintering the calcite in a CO_2 atmosphere to avoid decomposition. Their petrophysical characterization and properties were compared with natural ones and discussed.

2. MATERIALS AND METHODS

2.1. Fabrication of artificial core plugs

In a prior study from the group, several alternatives were tested, aiming to produce consolidated calcium carbonate parts (Morais et al., 2022). The two alternatives that had the best results were: 1) Partial sintering at a temperature below the decomposition temperature of calcium carbonate (Lin and Shen, 2013; Putri et al., 2020); and 2) Sintering the carbonate using a CO_2 atmosphere to increase the decomposition temperature (Criado et al., 1995; Monchau et al., 2013; Tarì and Ferreira, 1998);

The calcite used to produce the artificial rocks was a high-purity $CaCO_3$ powder (Êxodo Científica, Brazil) with a median agglomerate size of about 3.27 µm (measured by X-Ray monitored sedimentation with the Micromeritics SediGraph III Plus). The agglomerates were composed of needle-like nanocrystals of calcite (Figure S1 in the supplementary material). The true density of the powder was 2.7286 g/cm^3, and the BET surface area was 2.472 m^2/g (Quantachrome - Nova 1200e). The $CaCO_3$ powder was modified by adding 2 wt.% of a polyvinyl butyral as a binder and 0.2 wt.% of ethylene glycol as a plasticizer. The powder with the additives was dispersed in isopropyl alcohol in the weight proportion of approximately 3:4 and mixed in a roller ball mill for 2h. The mixture was dried with a hot air blower, granulated with mortar and pestle, and sieved with mesh ASTM #50 (300 µm).

2.1.1. Partial sintering with pure calcite

The first strategy was partial sintering at a temperature below the decomposition temperature of $CaCO_3$, which is about 525°C at 0.036 kPa of partial pressure of CO_2 (ambient condition) (Criado et al., 1995; Escardino et al., 2013; Viswanathan et al., 2010). Two types of samples were prepared using the modified calcite powder: 10 small cylinders (ø6 mm diameter) and one large core plug (ø41 mm diameter). First, the small cylinders (each with 0.5 g) and the core plug (with 90 g) were shaped by uniaxial compaction at 100 MPa in a manual hydraulic press in their respective cylindrical steel dies. Then, all samples were isostatically compacted at 190 MPa inside an evacuated and

sealed elastomer. Finally, the samples were partially sintered with a heating rate of 1°C/min up to 500-520°C and then kept at this temperature for at least 2h before cooling. The samples were cooled passively inside the furnace after it was turned off (> 8 h). The heat treatment removed the organic materials used to modify the powder. The partially sintered core plug is displayed in Figure 1.

Figure 1 – Partially sintered core plug. It was the only sample that used an aqueous solution of polyvinyl alcohol instead of polyvinyl butyral as the binder.

After partial sintering, the large plug was grinding machined to adjust the diameter and height to 1.5 inches using a ceramic CNC machining bench (designed and built in-house) (Figure S2 and S3). The height of the sample was adjusted with the sanding paper. The adjustment was necessary to fit the plug into the experimental equipment for nuclear magnetic resonance and permeability tests.

2.1.2. Sintering with CO_2 and pore formers

The second strategy was using a rich CO_2 atmosphere during sintering to increase the decarbonization temperature and achieve higher densities (Criado et al., 1995; Monchau et al., 2013; Tarì and Ferreira, 1998). Although the sintering process reduces the intrinsic porosity of the material (which is generally higher than 35% for compacted samples), it is necessary to increase the particle cohesion and the mechanical resistance of the part (Reed, 1995; Richerson and Lee, 2018). Therefore, a pore former was added to the calcite powder to promote the multiscale porosity, counteracting the porosity reduction promoted by the sintering process. A pore former (or porogen) is a sacrificial material with the desired pore shape and size, which is removed (by thermal oxidation, decomposition, dissolution, or sublimation) after the matrix material is consolidated (Chen et al., 2021; Colombo, 2006; Studart et al., 2006). Using pore formers allows tuning

the porosity, pore size distribution, and pore shape (Camilo et al., 2017; Chen et al., 2021; Monchau et al., 2013; Studart et al., 2006; Tikhonova et al., 2021). Ammonium bicarbonate ($(NH_4)HCO_3$) was selected as pore former because it thermally decomposes at low temperatures (≈ 36 to 60°C) into water vapor, carbon dioxide, and ammonia, leaving no residues.

The ammonium bicarbonate was manually grounded and classified by sieving into two sizes: Large (L) – smaller than mesh ASTM #50 (300μm) and larger than mesh ASMT #80 (180 μm); and Small (s) – smaller than mesh ASTM #170 (90 μm). Four different formulations were prepared according to Table 1. The mass of the porogen (m_p) in each composition was calculated according to Eq 1.

$$m_p = m_m \frac{\rho_p}{\rho_m} \frac{\phi}{1-\phi} \quad (1)$$

ϕ is the intended volumetric fraction of pores (porosity), m_m is the mass of the matrix material, ρ_p is the porogen density (ammonium bicarbonate) and ρ_m is the theoretical matrix density (calcite). The ammonium bicarbonate and calcite density were adopted as 1.57 and 2.71 g/cm^3, respectively. Each composition (calcite + porogen) was mixed for 20 min using a roller ball mill.

Sample Group	Porogen volume Vol.%	Porogen size μm	$(NH_4)HCO_3$ g	$CaCO_3$ with PVB g
5% L	5	180-300	9.3	300.7
10% L	10	180-300	18.9	291.1
20% L	20	180-300	39.6	270.4
20% s	20	< 90	39.6	270.4

Table 1 – Formulations of $CaCO_3$ with ammonium bicarbonate porogen.

For each formulation, 12 cylinders with ø 6 mm and 3 large plugs with ø 41 mm were shaped through uniaxial pressing at 100 and 75 MPa, respectively. Then, all samples were isostatically compacted at 190 MPa. Before sintering, the porogen was slowly removed from the samples in a heated chamber at 55°C for 4 weeks to avoid cracking the fragile calcite matrix with the evolved gases (Colombo, 2006; Studart et al., 2006). Caution must be taken for proper exhaustion of the evolved gases because ammonia has a strong odor that irritates the respiratory system.

Sintering was performed inside a tubular furnace (Figure 2). The construction of the tube was described elsewhere (Morais et al., 2022). Sintering was performed according to the heating program displayed in Table 2. Initially, compressed air was injected into the furnace at ≈ 3 L/min. Then, above 500°C, the gas flow was switched to CO_2 (≈ 3 L/min). Finally, the gas inlet was stopped after the temperature decreased to

500°C during cooling. The samples were cooled passively inside the furnace after it was turned off (> 12 h). The heat treatment removed the organic materials used to prepare the powder. Figure 3 displays some sintered artificial rocks produced with pore formers. The pores of the samples 5%L, 10%L, and 20%L were visible to the naked eye.

Step	Gas flow	T_{start} °C	T_{end} °C	Rate °C/min	Step time min	Total time min
1	Air	30	500	1	470	470
2	Air	500	500	-	120	590
3	CO_2	500	820	5	64	654
4	CO_2	820	850	2	15	669
5	CO_2	850	850	-	120	789
6	CO_2	850	500	furnace natural cooldown		
7	-	500	30			

Table 2 – Sintering program for $CaCO_3$ samples with ammonium bicarbonate.

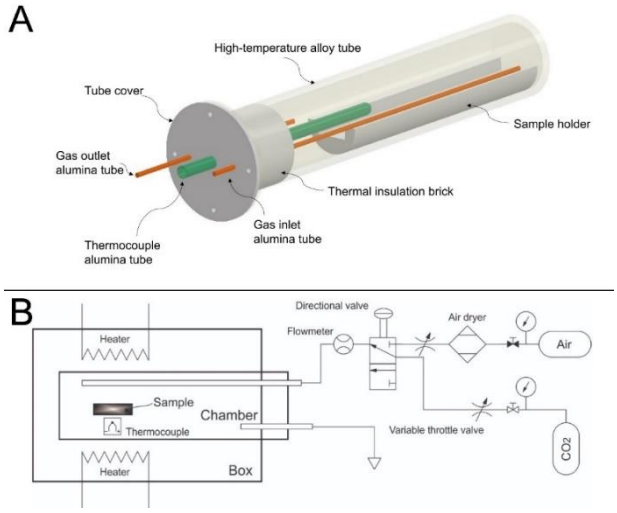

Figure 2 –Tubular furnace with controlled atmosphere flow. In A is the 3D design of the furnace. In B is the schematic representation of the technical components.

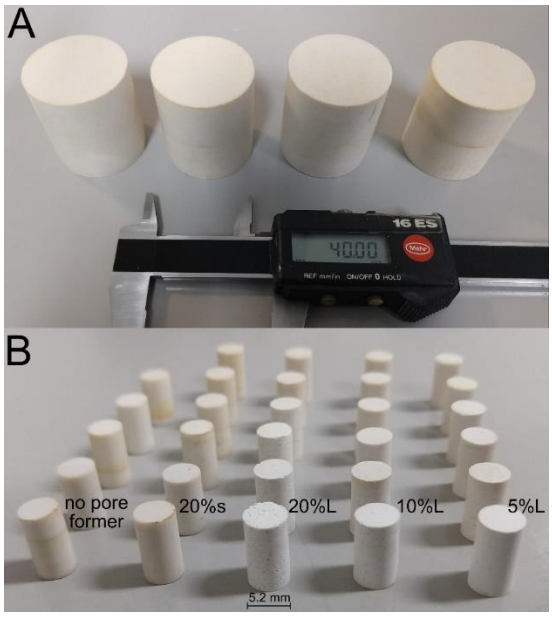

Figure 3 – Artificial rocks sintered with pore formers. A) 1.5 inches core plugs (one of each formulation). The caliper indicates 40 mm; B) Small cylinders from each formulation (and some samples without pore formers). The differences in the porosity were visible to the naked eye.

2.2. Characterization

2.2.1. X-Ray diffraction

The crystalline phases of the materials were evaluated using X-ray diffraction (XRD). The analyses were performed with the powder as supplied (pure calcite), after sintering at 520°C for 24h in air, after sintering at 850°C and 900°C for 2h in a CO_2 atmosphere. In addition, the effect of mixing the calcite powder with isopropyl alcohol and the organic binder was also evaluated with XRD before and after sintering. All analyses were conducted in the equipment Shimadzu XRD-7000 Maxima X with the following parameters: Cu K_α radiation, 40 kV, 30 mA, divergence and scatter slit of 1°, receiving slit of 0.3 mm, continuous scan θ-2θ with 2°/min ranging from 10 to 80°.

2.2.2. Porosimetry

The mass and dimensions of all samples were measured before and after sintering. Then, the volumetric bulk density was calculated ($\rho = m/V$). Additionally, the bulk and skeletal density of the two small cylindrical samples of each type of sample (3 for partially sintered samples) were measured by water immersion (Archimedes' principle) according to ASTM C373-18 (ASTM International, 2018). (The equations are available in the supplementary material). Finally, the skeletal density and close porosity of one small cylinder from each group (5%L, 10%L, 20%L, and 20%s) were calculated using a helium pycnometer (Micromeritics AccuPyc 1340), which is similar to a gas porosimeter. The closed porosity was calculated considering the theoretical density of fully densified calcite (the original powder) as 2.72 g/cm^3.

2.2.3. Microtomography and Scanning Electron Microscopy

One small cylinder of each porosity level (5%L, 10%L, 20%L, and 20%s) was analyzed using 3D microcomputed tomography (μCT) (Xradia Versa XRM-510) with 4.5 μm resolution (160 kV, 10W, 1000 projections, 10s exposure time, 2048x2048 pixels; saved as 16-bit unsigned TIFF format). Additionally, one partially sintered cylinder was also analyzed with 4.5 μm resolution using the 3D X-ray microtomography SKYSCAN 1272 (Bruker).

The μCT images of the samples with induced porosity were segmented and analyzed using PerGeos v1.0.1 according to the following steps: 1) The digital volumes were cropped into 3.15 mm edge cubes (of the central region of each sample); 2) The acquisition noise was filtered using the non-local means filter (search window 21; local neighborhood 5; similarity value 0.6; adaptative = true); 3) Manual thresholding was used to segment the pore and the matrix; 4) The pores were automatically separated and labeled using the tool *separate pore volume* (conservative chamfer method; 3D interpretation; Detect neighborhood edges; Marker extent 1; algorithm repeatable); 5) The equivalent diameter and volume distribution of the pores were recorded; 6) The pore structure was rendered using different colors for the separated pores.

One small cylinder of each porosity level (5%L, 10%L, 20%L, and 20%s) was polished and thermally etched for scanning electron microscopy (SEM). The partially sintered sample was only fractured. The samples were coated with carbon using the "BAL-TEC coating system (model SCD-50) equipped with a turbomolecular vacuum pump (EDWARDS T-STATION/75DXNW40)" (Barreto et al., 2019). The images were collected using a Dual Beam electron microscopy (FEI; Helios NanoLab 600i) with the following operating conditions: accelerating voltage of 2 kV, current of 11 pA, and Everhart-Thornley secondary electron (SE) detector.

2.2.4. Mercury injection porosimetry

Mercury injection porosimetry was performed on one small cylinder of each group (5%L, 10%L, 20%L, 20%s, and partially sintered) using the Porosimeter Model 5-7118 (American Instrument Company - AMINCO). The intrusion pressure was raised up to 5000 psi. The pore throat calculation adopted a surface tension of 0.485 N/m and a contact angle of 130° for the mercury/air interface. In addition, a complementary test was made with the porosimeter MicroActive AutoPore V 9600 (Micromeritics) with the samples 20%L and 20%s to verify if there was additional mercury intrusion up to 60,000 psi.

2.2.5. Permeability

The permeability of one large core plug from each sample type was evaluated using customized JBV core flooding equipment (serial number JBV-P101-0121). The permeability measurement was taken using water at a flow rate of 1 cm^3/min after injecting 5 pore volumes while ensuring pressure stabilization. Additionally, a back pressure of 1060 psi and a confining pressure of at least 1000 psi greater than the injection

pressure were applied. The differential pressure measured between the entry and sample plug outlet was used to calculate permeability, applying Darcy's Law.

2.2.6. Mechanical tests

The mechanical tests were performed using the universal testing machine MTS Bionix Model 370.02. The uniaxial compression test of the ø 6 mm cylindrical samples was based on ASTM C1424 – 15 (ASTM International, 2010) and ASTM C773 – 88 (ASTM International, 2020). The preload was set to 5 N, the crosshead approach speed to 5 mm/min, and the test speed to 0.3 mm/min. The room conditions during the experiment were 23.4 °C and 40% relative humidity. Eight samples from each group were tested (seven for the partially sintered samples).

2.2.7. Nuclear Magnetic Resonance (NMR)

The use of artificial rocks to calibrate logging tools was evaluated using Nuclear Magnetic Resonance (NMR). One large core plug (38 mm diameter) from each sample group was analyzed by NMR in a magnetic field of 0.047 T, which corresponds to the frequency of 1.95 MHz for ^{1}H atomic nuclei. The experiments were performed using a Redstone/Tecmag spectrometer.

The samples were evacuated and saturated with distilled water before the measurements. The width of the $\pi/2$ and π radiofrequency pulses were 13.6 µs and 27.2 µs, respectively. The recycle delay between scans was set to 10 s for all measurements.

Longitudinal (T_1) and transverse (T_2) relaxation times were obtained. T_2 was measured by the CPMG technique (Carr and Purcell, 1954; Meiboom and Gill, 2004). T_1 was measured using the Inversion Recovery (IR) technique with logarithmically spaced recovery times (Callaghan, 1993).

The partially sintered samples present only microporosity, resulting in the measurement of shorter T_2 relaxation times. Therefore, they were measured using echo time of 150 µs, employing 5000 echoes, and recovery times ranging from 0.1 ms to 100 ms. The other samples (5%L, 10%L, 20%L, and 20%s), which present longer T_2 relaxation time, were measured using echo time of 200 µs, employing 45000 echoes, and recovery times ranging from 0.1 ms to 6 s.

2.2.8. Core flooding with an acid solution – preliminary tests

Additionally, preliminary tests were made with one large plug of each group to evaluate the viability of core flooding experiments with acid injection (15 wt.% HCl + 1wt% Cl solution), 1 cm^3/min flow rate, and 1060 psi backpressure) using customized JBV equipment (serial number JBV-P-101-0121). The confining pressure was up to 4500 psi. After acid breakthrough and wormhole formation, the plugs were scanned in the μCT.

3. RESULTS AND DISCUSSION

The samples sintered in the CO_2 atmosphere at 850°C presented sensible differences compared to the partially sintered samples: the mechanical resistance and hardness increased, the external surface became smoother, and the color changed from a chalk-like white to a light brown/gray. The following sections present the characterization results of the artificial rocks.

3.1. Crystalline structure

The XRD of the partially sintered powder at 520°C for 24h in an air atmosphere revealed no traces of thermal decomposition, as only the calcite phase ($CaCO_3$) was detected (Figure 4, second diffractogram). In addition, pure calcium carbonate powder presented no mass loss at 520°C, confirming no decomposition occurred.

Similarly, no decomposition was detected for the samples sintered at 850°C in the CO_2 atmosphere (Figure 4, upper diffractogram). In fact, the diffraction peaks of calcite were even more intense and sharp, indicating higher crystallinity and crystallite growth (Ladd and Palmer, 2013; Leoni, 2019). However, signs of decomposition were detected for samples sintered at 900°C (Figure S4). It is known that the equilibrium temperature of the thermal decomposition of $CaCO_3$ at a CO_2 partial pressure of 1 atm (101.3 kPa) is about 895°C (Criado et al., 1995; Escardino et al., 2013; Someya et al., 1993; Valverde et al., 2015), which explains the beginning of the decomposition of the powder at 900°C. Therefore, the sintering temperature was limited to 850°C for all samples.

Finally, milling the calcite powder with polyvinyl butyral binder and isopropyl alcohol resulted in some traces of the aragonite phase (Figure S5). However, after sintering at 850°C, the XRD of the artificial rocks revealed only the calcite phase. Hence, the aragonite formed during milling was converted during heating to the more stable calcite phase (Stern and Weise, 1969).

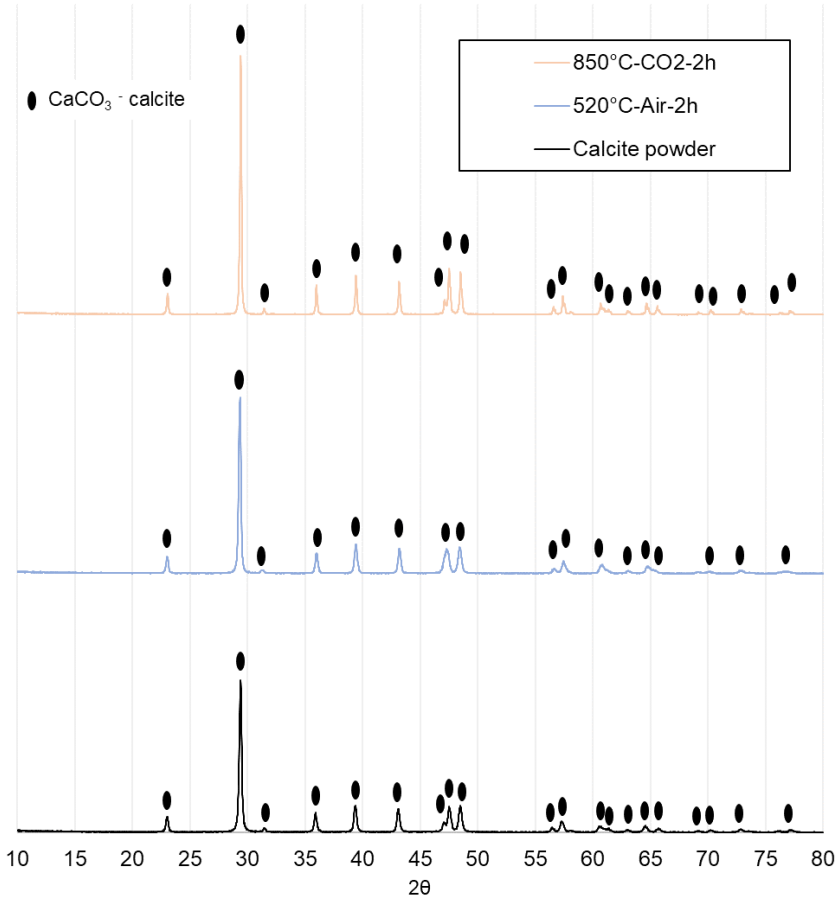

Figure 4 – X-Ray diffraction patterns.

3.2. Shrinkage, density, and porosity

Concerning the partially sintered samples, the average density of the ø6 mm cylinders was 1.8 ± 0.1 g/cm^3. The samples had a minor volumetric shrinkage (1.6-2.3%), indicating some particle rearrangement and initial binding but with minimal densification. Consequently, the intrinsic intergranular porosity was large (34.7% total porosity), despite having no pore former. Water intrusion (Archimedes' principle) revealed that the skeletal density was 2.56 g/cm^3 (4.1% closed porosity).

The samples with induced pores sintered in the CO_2 atmosphere presented about 27% of volumetric shrinkage during sintering, indicating a significant porosity reduction. The open and closed porosity of the samples from each formulation obtained by water intrusion (Archimedes' principle) is displayed in Figure 5. The total porosity is close to the planned porosity for each group. As expected, the porosity of the samples increased as the amount of pore former used increased. Furthermore, water intrusion revealed that the skeletal density of the sintered samples was between 2.67 and 2.69, corresponding to

1.0-1.4% of closed porosity (not connected). The reduced interparticle porosity was a consequence of the sintering process.

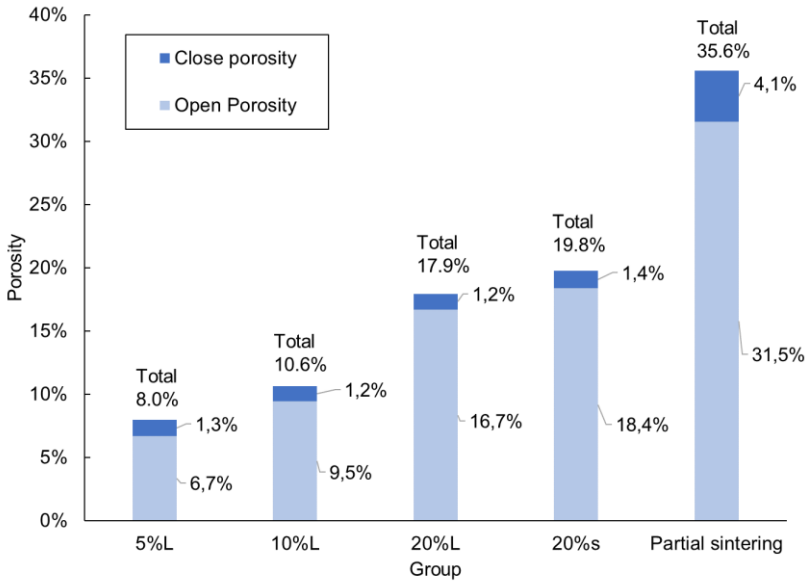

Figure 5 – Open and close porosity of artificial rocks (ø6 mm cylinders) obtained by water immersion.

Helium porosimetry (pycnometry) presented similar results (Table 3), with slightly higher density values (the gas permeates the samples more efficiently than water). In addition, it revealed that the connectivity of the pores increased as the amount of pore former increased (as expected).

		5%L	10%L	20%L	20%s
Skeletal density	g/cm^3	2.670	2.689	2.714	2.721
Close Porosity	%	1.8	1.2	0.2	0.0

Table 3 – Density and closed porosity obtained through helium pycnometry.

3.3. Pore structure: microtomography and scanning electron microscopy

The intrinsic pores of the partially sintered samples were smaller than 250 nm and only visible through scanning electron microscopy (Figure 6). Neither the optical microscope nor the µCT (Figure 7A) could detect the porosity. Although highly porous (>34%), the pores were smaller than the resolution of the µCT (4.5 µm). It is known that for samples with a homogeneous chemical constitution, the grayscale distribution is proportional to the density, which is linearly related to the microporosity of the sample (Ji et al., 2015, 2012). The grayscale histogram of the µCT image (Figure 7B) has a region centered at 174 related to the material signal. This region was considered homogeneous due to the monomodal distribution shape. Therefore, it indicates a homogenous density

distribution in the scale of observation by the µCT. Although the µCT image presented some concentric ring artifacts around the rotation center, those are related acquisition process and not to the sample.

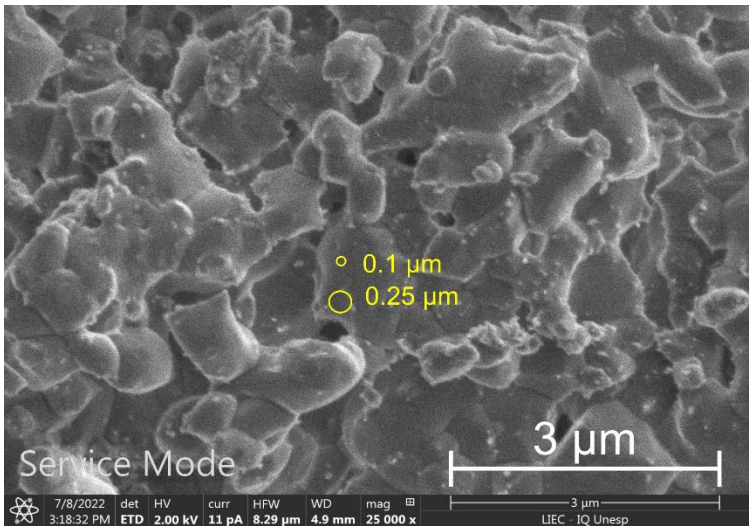

Figure 6 – Scanning electron microscopic image of the partially sintered sample. Yellow circles are displayed for comparison with pore diameters.

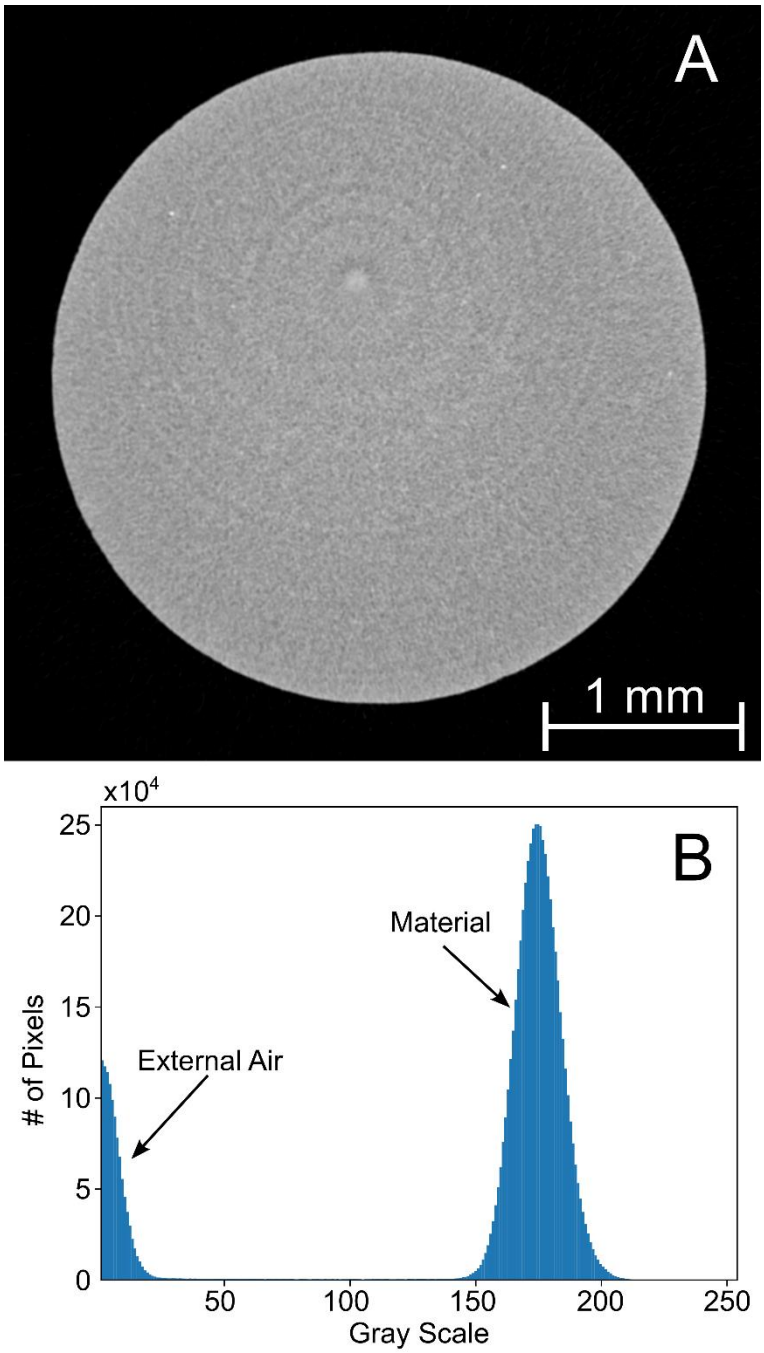

Figure 7 – Microtomography of partially sintered samples. A) Microtomography slice with resolution 4.5 µm of a partially sintered sample without any visible porosity. The concentric circles are ring artifacts that could not be completely filtered out during reconstruction. B) Gray-level histogram of the image.

Concerning the samples with pore formers, Figure 8 presents the rendering of the pores obtained through µCT after segmentation and separation. The cumulative pore size distribution (weighted by pore volume) is presented in Figure 9. Both images show evident differences between the samples. The calculated porosity data is displayed in Table 4. As expected, the total porosity increases with the amount of pore former used during the fabrication. Furthermore, the average pore size was proportional to the size of

the pore former used. Additionally, the average equivalent pore diameter in the µCT images matches the pore size observed in the scanning electron microscopy (Figure 10).

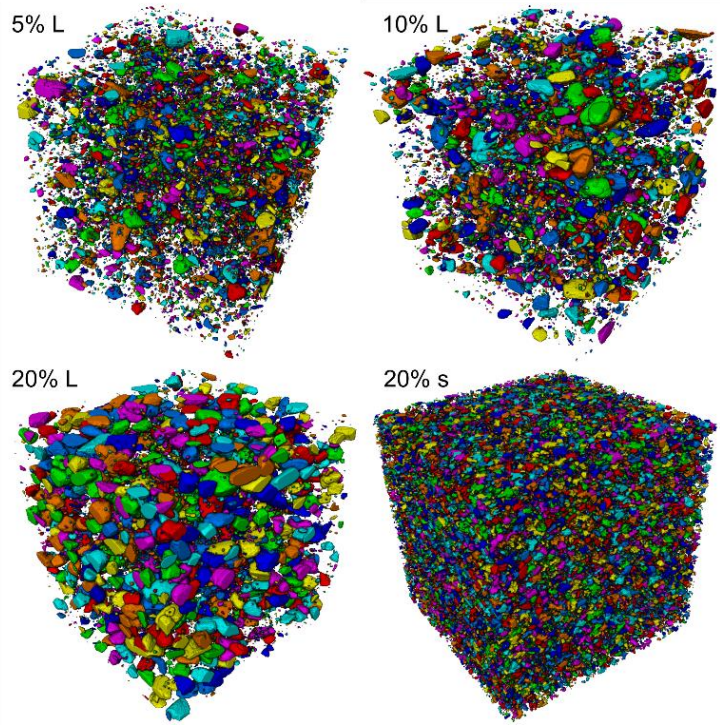

Figure 8 – Pores obtained after segmentation and separation in the software PerGeos. Each cube has a 3.15 mm edge.

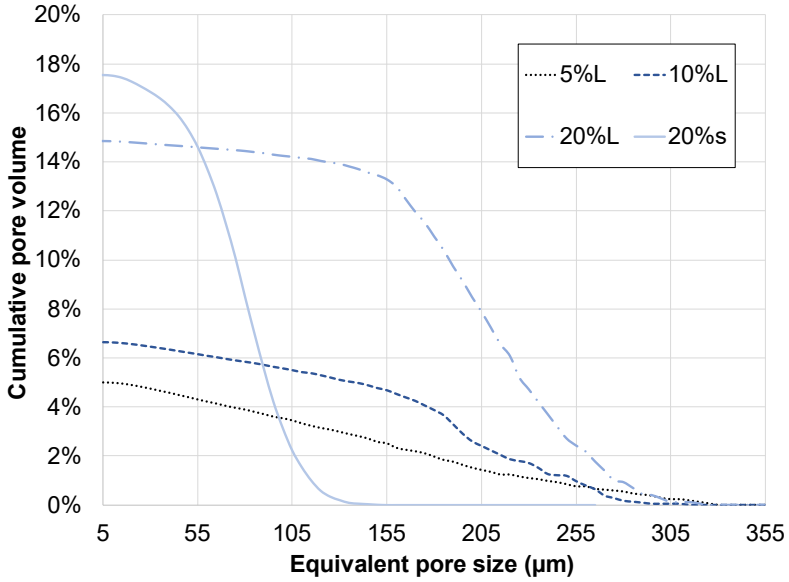

Figure 9 – Cumulative pore volume as a function of the minimum equivalent diameter.

		5%L	10%L	20%L	20%s
Porosity only internal	%	3.98	4.8	7.33	4.05
Porosity connected to external faces	%	1.03	1.8	7.53	13.51

Porosity (µCT)	%	5.0	6.6	14.9	17.6
"Invisible" porosity	%	3.1	2.7	4.9	1.5
Total porosity (volumetric)	%	8.1	9.4	19.8	19.1
Average pore size (volume weighted)	µm	162.1	183.6	211.3	83.0
Max pore size	µm	334.5	315.4	328.9	158.7

Table 4 – Porosity data measured through µCT. The total porosity was measured volumetrically, and the intrinsic porosity is the difference between the total porosity and the porosity calculated using the µCT images.

As expected, as the porosity increases, the connectivity also increases, as evidenced by the overlapping pores forming larger pore clusters in the scanning electron microscopy images (white arrows in Figure 10) and the increased fraction of porosity connected to the external edges (Table 4). In addition, the slight increase in average pore size with increased porosity (Table 4) is also related to the interconnected pores that were computed as bigger pores in the µCT.

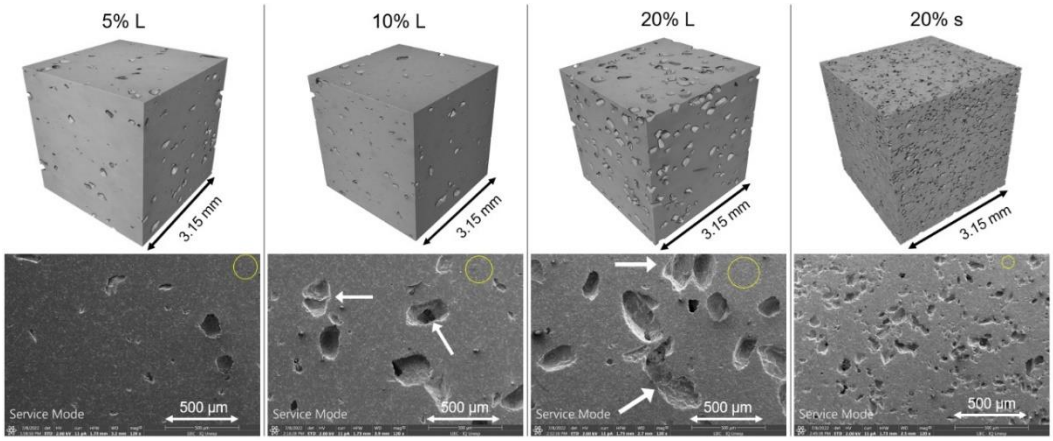

Figure 10 – Comparison between microtomography and scanning electron microscopy images. Above are the rendered 3D images obtained from µCT (each cube has a 3.15 edge). Below are the scanning electron microscopy images (120x magnification). The yellow circle in the upper right corner of each microscopy represents the average pore size calculated in the µCT. The arrows point to connected pores.

Two types of pores were identified in the samples: the large induced pores (micrometric) generated by the pore formers (ammonium bicarbonate) and the intrinsic porosity (nanometric pores and intergranular fractures) resulting from the compaction process. The intrinsic porosity was invisible at the µCT resolution but revealed during the scanning electron microscopy (Figure 11). This "invisible" porosity is why the porosity calculated using the µCT is lower than the actual porosity. The sintering process at 850°C reduced the intrinsic porosity compared to the partially sintered samples (Figure 6), which have an "invisible" porosity of more than 34%. The bimodal porosity produced in the artificial samples with porogen is suitable to represent the hierarchical porosity of carbonate rocks. The "invisible" intrinsic porosity can be related to the intergranular and

intercrystalline porosity in carbonates, while the larger induced pores can be related to vuggy porosity (Schön, 2011).

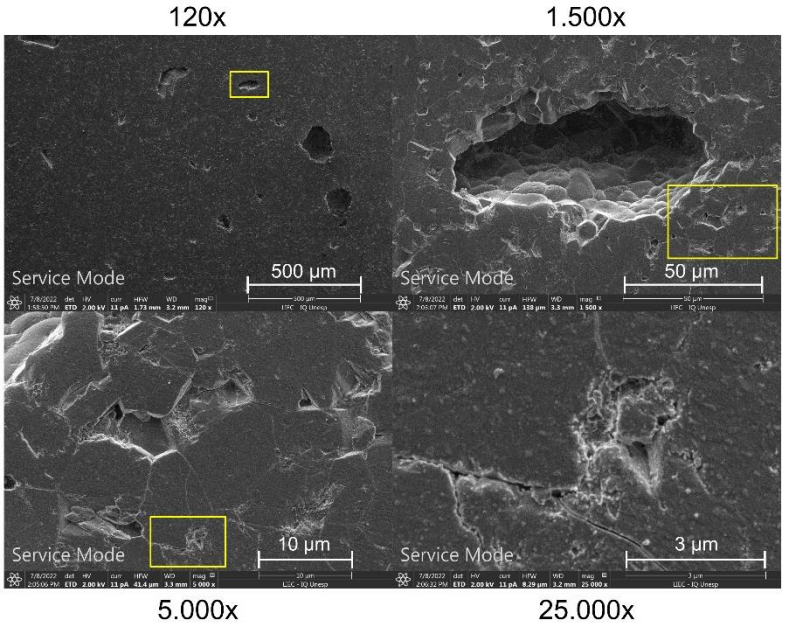

Figure 11 – Scanning Electron Microscopic images of the same 5% L sample with increasing magnification. The yellow boxes display the region magnified in the following image.

3.4. Mercury injection porosimetry

The results of the mercury injection porosimetry are displayed in Figure 12 and Table 5. The mercury intrusion on the sample 5%L was negligible and lower than the minimum resolution of the equipment. In the complementary experiment, no additional intrusion was observed for samples 20%L and 20%s between 5 and 60 kpsi (3-36 nm), indicating that the remaining pore throats are below 3 nm.

The difficulty for the mercury to penetrate in such narrow channels explains why the injected volume on samples 5%L, 10%L, and 20%L was significantly lower than their porosity. Furthermore, many of the inter and intra-granular pores were closed and not connected to the exterior of the samples. On the other hand, the large intrinsic porosity of the partially sintered sample enhances the connectivity of the pores, allowing a higher mercury intrusion, despite the smaller pores. Finally, the sample 20%s showed an intermediate behavior. It has smaller pores and pore throats than samples 20%L, but the pores are more connected, resulting in larger mercury intrusion for pressures up to 5 kpsi.

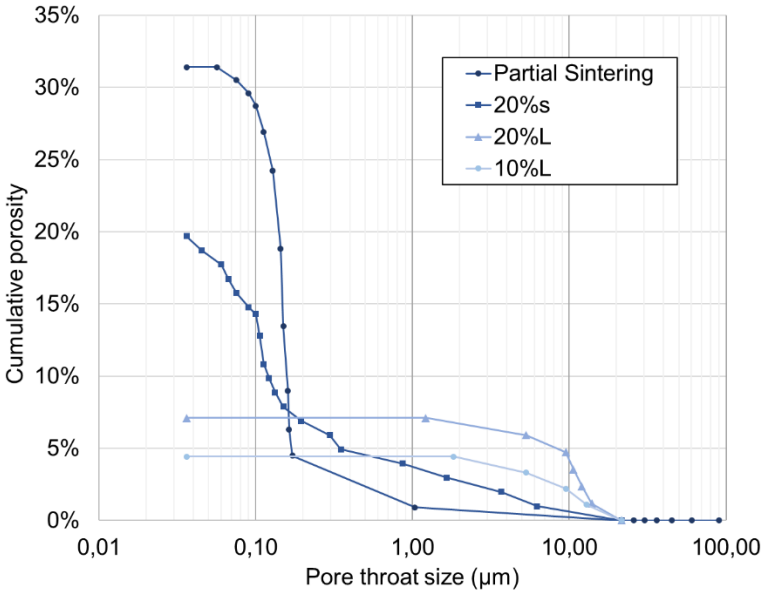

Figure 12 – Mercury injection porosimetry.

		PS	5% L	10% L	20% L	20% s
Skeletal density (pycnometry)	g/cm^3	---	2.67	2.69	2.71	2.72
Avg. pore diameter (µCT)	µm	---	162.1	183.6	211.3	83.0
10% of pore throats smaller than (d10)	µm	0.10	---	3.22	3.68	0.06
Median pore throat diameter (d50)	µm	0.15	---	9.52	10.64	0.12
90% of pore throats smaller than (d90)	µm	0.17	---	18.09	16.96	3.69
Porosity (volumetric)	%	34.7	7.3	10.3	17.6	19.4
Open porosity (Archimedes' principle)	%	31.4	6.4	9.7	16.1	18.4
Volume of mercury injected	%	31.4	---	4.4	7.1	19.9

Table 5 – Mercury injection porosimetry results compared.

3.5. Permeability

The permeability results are presented in Table 6. Furthermore, Figure 13 shows the porosity *vs.* permeability relation of the artificial rocks measured in this study compared with some literature results for natural (Baud et al., 2017; Heap et al., 2018; Regnet et al., 2015; Zakaria et al., 2015) and artificial carbonate rocks (Fedrizzi et al., 2018; Florez and Ferrari, 2021; Zakaria et al., 2015). It can be seen that the permeability of the proposed artificial rocks produced in this study is comparable to some natural rocks of very low permeability.

Sample	Unit	Partial sintering	5%L	20%L	20%s
Permeability (flow)	mD	0.049	0.057	0.051	0.058

Table 6 – Permeability of the artificial carbonate plugs. The sample with 10% porosity had to be discarded due to a crack (Figure S6 in the supplementary material).

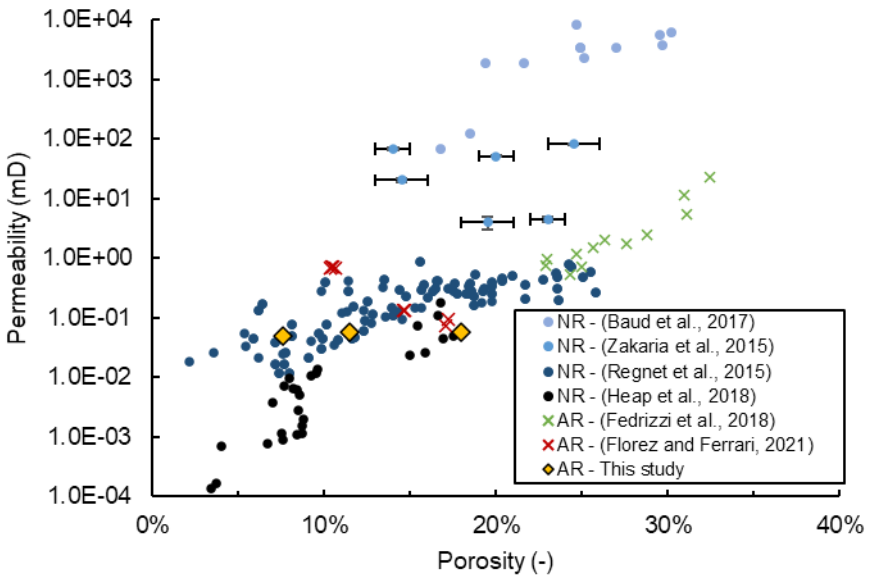

Figure 13 – Porosity *vs.* permeability relationship for the artificial rocks (AR) and some natural carbonate rocks (NR) in the literature (Baud et al., 2017; Fedrizzi et al., 2018; Florez and Ferrari, 2021; Heap et al., 2018; Regnet et al., 2015; Zakaria et al., 2015). The data is included in the Supplementary Material Table ST1.

Although the high porosity of the partially sintered samples (>34%), the small particle size (<1µm) used for the fabrication of the artificial rocks resulted in tiny pore throats, which explains the low permeability of the samples (Schön, 2011). The samples with induced pores sintered in the CO_2 atmosphere also presented low permeability. Despite the large induced pores, the pore throats were very small (revealed by the mercury injection porosimetry) and poorly connected. The intrinsic porosity between the large pores was the "bottleneck" of the flow, reducing the permeability.

3.6. Mechanical resistance

Concerning the mechanical tests, the results are summarized in Figure 14. As observed, the scattering in the results is substantial. It is caused by the typical dispersion of the strength of brittle materials and the presence of defects and stress concentrators (such as the induced pores and cracks).

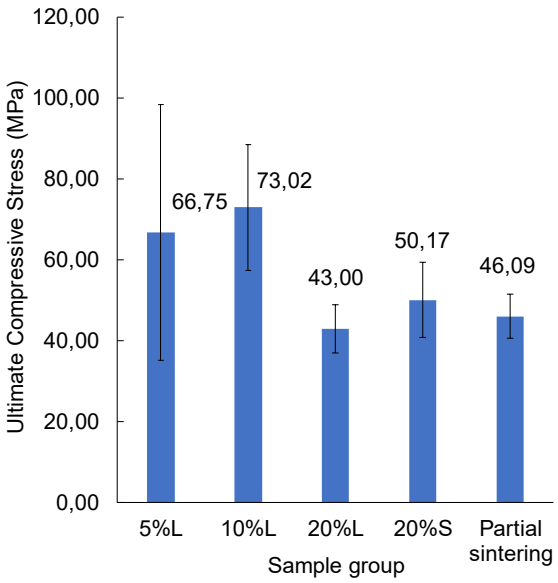

Figure 14 – Average ultimate compressive stress of the calcium carbonate samples. Error bars represent ± one standard deviation. The data is included in the Supplementary Material Table ST2.

Figure 15 compares the strength of the artificial rocks with some natural rocks reported in literature. As can be seen, the ultimate compressive stress of the artificial rocks was very similar to the strength of natural carbonate rocks (13-400 MPa), especially those with similar porosity (Baud et al., 2016; Van Stappen et al., 2019; Yasar and Erdogan, 2004; Zhu et al., 2010). One of the 5%L samples reached up to 126 MPa. Furthermore, the samples could withstand water immersion for more than 48h without any signal of crumbling or disintegration, highlighting the strong consolidation of the particles.

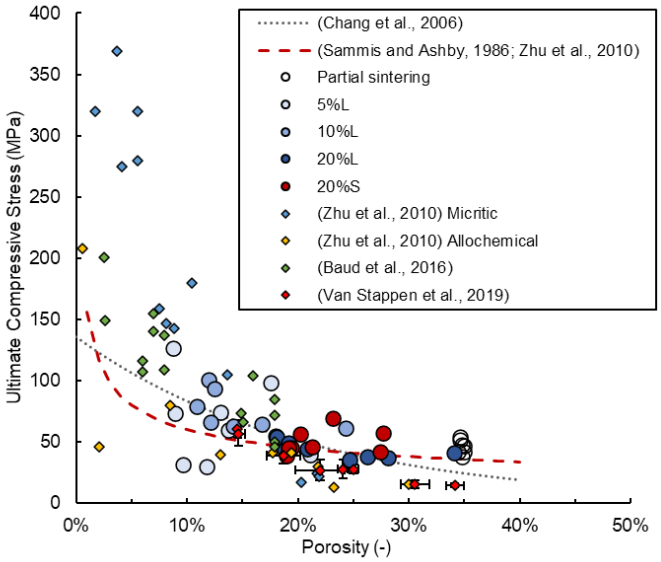

Figure 15 – Ultimate compressive stress of each sample compared with natural carbonate rocks in literature and with compression strength models. The data is included in the Supplementary Material Table ST3.

It should also be noted that there is a general tendency both for natural and artificial rocks that as the porosity increases, the mechanical resistance decreases. Although the dispersion, the data was reasonably described by the model in Eq. 2 (Chang et al., 2006), where *UCS* is the unconfined (ultimate) compressive strength and ϕ is the sample porosity.

$$UCS = 135.9 \exp(-4.8\phi) \quad (2)$$

Another model was proposed by Sammis and Ashby (Sammis and Ashby, 1986), which can be numerically approximated by Eq. 3 (Zhu et al., 2010). This model also considers the average pore radius *r* and the fracture toughness of the material K_{IC}. In this work, the K_{IC} was assumed 0.2 MPa $m^{1/2}$, which is the value measured for calcite (Zhu et al., 2010).

$$UCS = \frac{1.325}{\phi^{0.414}} \frac{K_{IC}}{\sqrt{\pi r}} \quad (3)$$

This model could describe well the data for the samples 20%s with an average pore diameter of 83 µm (obtained from µCT measurement). However, for the sample with larger pores (average diameter of 180 µm), the model underestimates the strength (not shown in the graph). It can be the case that the fracture mechanism is distinct for the larger pores or that the apparent fracture toughness K_{IC} can be different depending on the degree of sintering and the presence of nano and micropores. The use of the artificial rocks AS proposed in this study would allow a deeper understanding of the effects of porosity and pore size on the mechanical strength of carbonate rocks, as each variable can be controlled independently. A proper investigation of the porosity x compressive strength models is beyond the scope of this paper and is suggested for future works.

3.7. Nuclear magnetic resonance (NMR)

NMR revealed that the partially sintered porosity is monomodal (single peak) with T_2 at about 10 ms (Figure 16). It is known that the T_2 is proportional to the pore size (Brownstein and Tarr, 1979); Considering a high surface relaxivity of 50 µm/s (Lucas-Oliveira et al., 2020), the estimated pore size is 1.5 µm. Therefore, the small pore size confirms why the porosity was invisible at the µCT resolution.

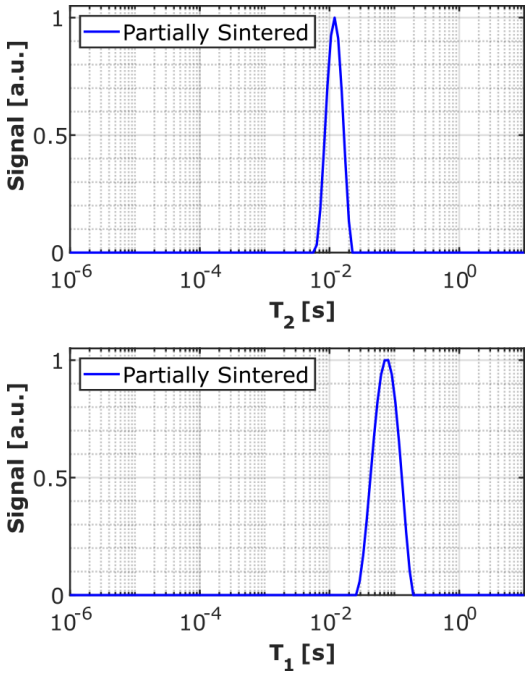

Figure 16 – NMR relaxation times (T_2 and T_1) of the partially sintered plug. The sample has a monomodal pore size.

For the samples with induced pores (Figure 17), the T_2 relaxation times revealed that the samples present bimodal porosity (two peaks indicating pores of different sizes). The large peaks on the right of each curve represent the pores induced by the porogenic agents. The small peaks on the left represent the intrinsic cracks and intergranular porosity not removed by sintering (barely noticeable for the 20%S sample due to the wider pore size distribution) (D'Eurydice et al., 2016). When comparing the 5%L, 10%L, and 20%L samples, the porosity change is evidenced by the height of the peaks on the right, both for the T_2 and T_1 measurements. Furthermore, the formation of larger pore clusters shifts T_2 to larger values as the porosity increases. Comparing the 20% L and 20% S samples, the peak shift for much shorter relaxation times identifies the change in pore size. Because the 20% S sample has a wider porogen size distribution than the 20% L sample, it results in a broader and lower intensity peak.

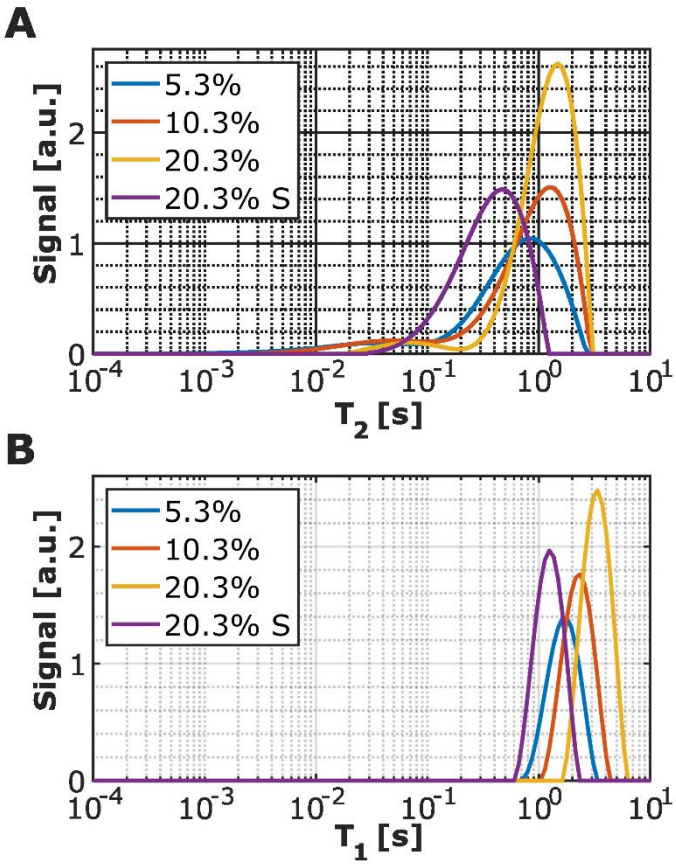

Figure 17 – NMR relaxation time T_2 and T_1 obtained by CPMG technique for the samples with induced pores.

Because samples had the same material (pure calcite), it was possible to evaluate the individual effect of each variable (porosity and pore size). Furthermore, the constant of proportionality between T_2 and pore size could be quantified as the surface relaxivity of the pores was the same for all samples (same material). These achievements were only possible due to using artificial carbonate rocks with controlled chemical constitutions and tunable pore structures. This advantage of artificial rocks can be used in other experiments to calibrate well-logging tools and to explore the individual effect of each variable in petrophysical characterization tests.

3.7.1. Core flooding with an acid solution

Finally, preliminary core flooding experiments with acid were successfully performed (Figure 18, S7, and S8). Core flooding with acid is one of the most challenging experiments concerning the mechanical resistance of the part. Previous attempts to produce artificial rocks failed to produce samples with sufficient strength to withstand such tests (Florez et al., 2019; Ishutov et al., 2017; Kong, 2019). Otherwise, they used

other materials besides calcium carbonate to achieve reasonable resistance, compromising the chemical purity (Fedrizzi et al., 2018; Florez and Ferrari, 2021; Wang et al., 2017). Therefore, the success of the fabrication strategy proposed is an important advance toward enabling the use of artificial rocks made entirely of calcium carbonate in the most challenging experiments.

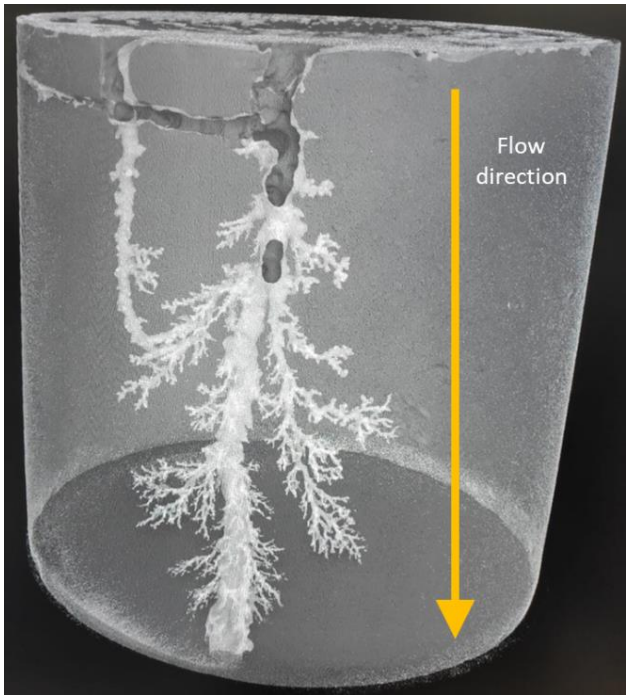

Figure 18 – Microtomography of the partially sintered core plug with a wormhole generated after core flooding with an acid solution.

3.8. Overall consideration of the process: challenges and opportunities.

One of the main advantages of artificial carbonate rocks is that they can have much more controlled properties and chemical composition than their natural counterparts. The proposed fabrication process is very versatile and can be adjusted to produce artificial rocks with different properties by A) varying the sintering temperature and time to control the intrinsic porosity; B) using pore former with multiples sizes to fine-tune the connectivity and permeability; C) changing the shape of the pore formers (spherical, fibers, disks) and D) compact samples with layers with different amounts of pore formers to induce anisotropic properties; E) Mix small amounts of impurities that alter the petrophysical experiments (such as ferromagnetic particles) (Figure 19).

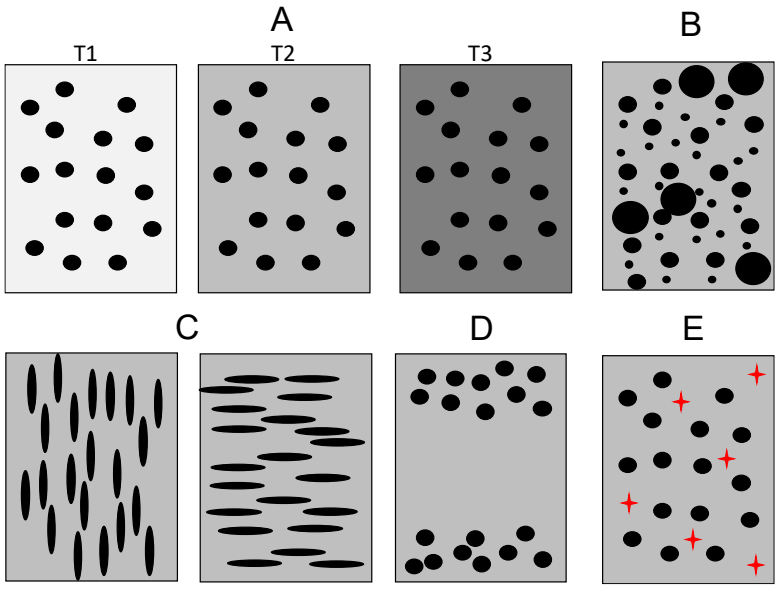

Figure 19 – Suggestions for future experiments. A) Changing sintering temperature and time; B) Adding pore formers with multiple sizes; C) Changing pore former size and orientation; D); Compacting samples with heterogeneous layers; E) Adding impurities particles.

Another promising path is producing artificial carbonate rocks with other compositions besides calcite. Natural carbonaceous rocks are usually not pure calcite but have a variable ratio of dolomite ($CaMg(CO_3)_2$) (Kushnir et al., 2015). Therefore, the possibility of sintering porous core plugs with a controlled percentage of dolomite would be of great scientific interest, especially for acid stimulation and enhanced oil recovery studies. However, dolomite has decarbonation and sintering temperatures different from calcite (Olszak-Humienik and Jablonski, 2015; Subagjo et al., 2017), increasing the complexity of the process. Although the authors have made some preliminary tests to evaluate the sinterability of core plugs with controlled dolomite fraction, more studies are required.

Regarding the fabrication costs, the raw materials calcium carbonate and ammonium bicarbonate are very cheap (less than 5 dollars/kg). Similarly, CO_2 is also not expensive (less than 2.5 dollars/kg). The main costs are from the infrastructure (ball mill, molds, uniaxial press, isostatic press, and the furnace with a controlled atmosphere). Hence, the process can produce parts at low to moderate costs. Furthermore, the partial sintering strategy is considerably cheaper, as it does not demand a furnace with a special atmosphere.

One of the limitations of the presented process is the low permeability achieved (0.05-0.06 mD). It was observed that interparticle porosity plays a key role in the permeability of the samples. The presence of larger pores (“vuggy porosity”) is not

enough to achieve a high permeability if they are not well connected by the intrinsic microporosity. For future developments, the permeability could be increased by 1) using larger particles as starting raw material (which would result in larger interparticle porosity), 2) reducing the sintering temperature and time to reduce densification, and 3) mixing small and large pore formers to enhance the connectivity of the pores. Finally, another possible route is combining this technic with additive manufacturing of calcium carbonate (Morais et al., 2023). The addition of the porogens can tune up the microporosity, while additive manufacture can create interconnected channels and larger pores.

4. CONCLUSIONS

Artificial carbonate rocks were successfully produced by compacting calcite powder with a pore former (ammonium bicarbonate) and sintering in a CO_2 atmosphere to avoid carbonate decomposition. The artificial core plugs presented chemical constitution, mechanical resistance, pore size, and porosity similar to natural ones. Partial sintering at 500°C is also a viable route that does not require a special atmosphere. However, it resulted in larger porosity (minimum of 34%) and smaller mechanical resistance than the fully sintered rocks.

The core plugs produced could withstand water immersion and be submitted to demanding petrophysical tests, including mercury injection porosimetry, nuclear magnetic resonance, and core flooding with an acid flow. To the best of the authors' knowledge, there are no reports in the literature of synthetic samples of pure calcium carbonate that have supported all these tests, highlighting the advances of the present work.

One of the significant advantages of the proposed process is the possibility of tuning the total porosity and pore size, controlling the resultant petrophysical properties in a reproducible way without compromising the chemical constitution. Therefore, the effect of each variable can be explored individually in petrophysical experiments. Furthermore, the reproducibility of the artificial rocks is especially suited for destructive experiments that require many samples, reducing the experimental scattering of the results. However, although high porosity was achieved, their pore throats were small and

poorly connected, which resulted in low permeabilities (0.05-0.06 mD). The process still requires improvements to achieve higher permeabilities.

The proposed fabrication method is simple, flexible, reproducible, and has low to moderate costs. In addition, these artificial rocks create new opportunities for research as they can be used in several applications in the oil and gas research field, such as testing different conditions for acid stimulation, evaluating surfactants for enhanced oil recovery, calibrating well-logging tools (NMR, ultrasonic, gamma ray…), and validating numerical simulations.

ACKNOWLEDGEMENTS

We would like to acknowledge MSc. Walter Mariano from Federal University of São Carlos (UFSCar), MSc. Rogério Erbereli from University of São Paulo (USP), and MSc. Elaine Araújo from the Federal University of Rio Grande do Norte (UFRN) for their valuable aid with the technical discussions and experimental support. We would like to acknowledge Prof. Rafael Salomão from USP for granting access to the BET facilities and the technical discussions. We also would like to thank LMA-IQ from UNESP for FEG-SEM facilities and the Laboratory of Technological Characterization (LCT) from USP for the µCT and pycnometry facilities. **Funding:** This work was supported by the São Paulo Research Foundation (FAPESP) [grants # 2020/16012-1 and #2009/54880-6], the National Council for Scientific and Technological Development, Brazil (CNPq) [grants #140797/2020-3 and #308076/2018-4], and the National Agency of Petroleum, Natural Gas and Biofuels, Brazil (ANP)/PETROBRAS [grant # 2020/00010-0].

DATA AVAILABILITY

The data that support the findings of this study are available from the corresponding author, M.M. Morais, upon request.

CRediT AUTHOR STATEMENT

Mateus M Morais: Conceptualization; Experimental investigation; Writing: original draft; **Everton L de Oliveira**: Conceptualization; Experimental investigation (NMR and µCT); Writing (Reviewing & editing); **Tito J Bonagamba**: Supervision; Resources; Funding acquisition; **Pedro TP Aum**: Conceptualization; Resources; Writing (Reviewing & editing); **Cláudio RS Lucas**: Experimental investigation (Core flooding

and permeability); **Daniel NN da Silva**: Experimental investigation (Core flooding and permeability); Writing (Reviewing & editing); **Carlos A Fortulan**: Writing (Reviewing & editing); Supervision; Project administration.

DECLARATION OF COMPETING INTEREST

The authors declare that they have no known competing financial interests or personal relationships that could have appeared to influence the work reported in this paper.

REFERENCES

Albalawi, H.I., Khan, Z.N., Valle-Pérez, A.U., Kahin, K.M., Hountondji, M., Alwazani, H., Schmidt-Roach, S., Bilalis, P., Aranda, M., Duarte, C.M., Hauser, C.A.E., 2021. Sustainable and Eco-Friendly Coral Restoration through 3D Printing and Fabrication. ACS Sustain Chem Eng 9, 12634–12645. https://doi.org/10.1021/acssuschemeng.1c04148

Almetwally, A.G., Jabbari, H., 2020. Experimental investigation of 3D printed rock samples replicas. J Nat Gas Sci Eng 76, 103192. https://doi.org/10.1016/j.jngse.2020.103192

Alyafei, N., 2021. Fundamentals of Reservoir Rock Properties - 2nd edition, Fundamentals of Reservoir Rock Properties. Hamad bin Khalifa University Press (HBKU Press). https://doi.org/10.5339/Fundamentals_of_Reservoir_Rock_Properties_2ndEdition

ASTM International, 2020. ASTM C773-88 Standard Test Method for Compressive (Crushing) Strength of Fired Whiteware Materials. https://doi.org/10.1520/C0773-88R20.2

ASTM International, 2018. ASTM C373-18, Standard Test Methods for Determination of Water Absorption and Associated Properties by Vacuum Method for Pressed Ceramic Tiles and Glass Tiles and Boil Method for Extruded Ceramic Tiles and Non-tile Fired Ceramic Whiteware Products. West Conshohocken, PA. https://doi.org/10.1520/C0373-18

ASTM International, 2010. ASTM C1424 -15 Standard Test Method for Monotonic Compressive Strength of Advanced Ceramics at Ambient Temperature. https://doi.org/10.1520/C1424-15R19

Baker, R.O., Yarranton, H.W., Jensen, J.L., 2015a. Rock and Fluid Properties, in: Practical Reservoir Engineering and Characterization. Elsevier, pp. 35–66. https://doi.org/10.1016/B978-0-12-801811-8.00002-X

Baker, R.O., Yarranton, H.W., Jensen, J.L., 2015b. Conventional Core Analysis–Rock Properties, in: Practical Reservoir Engineering and Characterization. Elsevier, pp. 197–237. https://doi.org/10.1016/B978-0-12-801811-8.00007-9

Barreto, J., Tita, D., Orlandi, M., 2019. DEVELOPMENT OF AN AUTOMATED METHOD TO PERFORM A QUANTITATIVE STUDY OF PARTICLE SIZE DISTRIBUTION AND THE EFFECT OF A CONDUCTIVE LAYER IN SCANNING ELECTRON MICROSCOPY. Quim Nova. https://doi.org/10.21577/0100-4042.20170353

Baud, P., Exner, U., Lommatzsch, M., Reuschlé, T., Wong, T., 2017. Mechanical behavior, failure mode, and transport properties in a porous carbonate. J Geophys Res Solid Earth 122, 7363–7387. https://doi.org/10.1002/2017JB014060

Baud, P., Rolland, A., Heap, M., Xu, T., Nicolé, M., Ferrand, T., Reuschlé, T., Toussaint, R., Conil, N., 2016. Impact of stylolites on the mechanical strength of limestone. Tectonophysics 690, 4–20. https://doi.org/10.1016/j.tecto.2016.03.004

Brownstein, K.R., Tarr, C.E., 1979. Importance of classical diffusion in NMR studies of water in biological cells. Phys Rev A (Coll Park) 19, 2446–2453. https://doi.org/10.1103/PhysRevA.19.2446

Callaghan, P.T., 1993. Principles of Nuclear Magnetic Resonance Microscopy. Oxford University Press.

Camilo, C.C., Silveira, C.A.E., Faeda, R.S., De Almeida Rollo, J.M.D., Purquerio, B.D.M., Fortulan, C.A., 2017. Bone response to porous alumina implants coated with bioactive materials, observed using different characterization techniques. J Appl Biomater Funct Mater 15, e223–e235. https://doi.org/10.5301/jabfm.5000347

Carbillet, L., Heap, M.J., Baud, P., Wadsworth, F.B., Reuschlé, T., 2022. The Influence of Grain Size Distribution on Mechanical Compaction and Compaction Localization in Porous Rocks. J Geophys Res Solid Earth 127, 1–22. https://doi.org/10.1029/2022JB025216

Carbillet, L., Heap, M.J., Baud, P., Wadsworth, F.B., Reuschlé, T., 2021. Mechanical Compaction of Crustal Analogs Made of Sintered Glass Beads: The Influence of Porosity and Grain Size. J Geophys Res Solid Earth 126. https://doi.org/10.1029/2020JB021321

Cardoso, C., Lucas, E., Uwe, B., Alberto, C., José, T., 2018. A model system based on synthetic rocks for morphological studies in porous media, in: Proceeding of the 14th International Bologna Conference on Magnetic Resonance in Porous Media (MRPM14). Gainesville, Florida, USA, p. P3.

Carr, H.Y., Purcell, E.M., 1954. Effects of Diffusion on Free Precession in Nuclear Magnetic Resonance Experiments. Physical Review 94, 630. https://doi.org/10.1103/PhysRev.94.630

Chang, C., Zoback, M.D., Khaksar, A., 2006. Empirical relations between rock strength and physical properties in sedimentary rocks. J Pet Sci Eng 51, 223–237. https://doi.org/10.1016/j.petrol.2006.01.003

Chen, Y., Wang, N., Ola, O., Xia, Y., Zhu, Y., 2021. Porous ceramics: Light in weight but heavy in energy and environment technologies. Materials Science & Engineering: R 143, 100589. https://doi.org/10.1016/j.mser.2020.100589

Choquette, P.W., Pray, L.C., 1970. Geologic Nomenclature and Classification of Porosity in Sedimentary Carbonates. American Association of Petroleum Geologists Bulletin 54, 207–250.

Colombo, P., 2006. Conventional and novel processing methods for cellular ceramics. Philosophical Transactions of the Royal Society A: Mathematical, Physical and Engineering Sciences 364, 109–124. https://doi.org/10.1098/rsta.2005.1683

Criado, J.M., González, M., Málek, J., Ortega, A., 1995. The effect of the CO2 pressure on the thermal decomposition kinetics of calcium carbonate. Thermochim Acta 254, 121–127. https://doi.org/10.1016/0040-6031(94)01998-V

Darling, T., 2005. BASICS, in: Well Logging and Formation Evaluation. Elsevier, pp. 1–27. https://doi.org/10.1016/B978-075067883-4/50001-2

Dautriat, J., Gland, N., Dimanov, A., Raphanel, J., 2011. Hydromechanical behavior of heterogeneous carbonate rock under proportional triaxial loadings. J Geophys Res 116, B01205. https://doi.org/10.1029/2009JB000830

de Castro Dantas, T.N., de Oliveira, A.C., de Souza, T.T.C., dos Santos Lucas, C.R., de Andrade Araújo, E., Aum, P.T.P., 2020. Experimental study of the effects of acid microemulsion flooding to enhancement of oil recovery in carbonate reservoirs. J Pet Explor Prod Technol 10, 1127–1135. https://doi.org/10.1007/s13202-019-00754-x

de Melo, L.M.P., 2012. ANÁLISE NUMÉRICO-EXPERIMENTAL DE ROCHAS CARBONÁTICAS SINTÉTICAS SUBMETIDAS À INJEÇÃO DE UM FLUIDO REATIVO. Universidade Federal de Pernambuco.

D'Eurydice, M.N., Montrazi, E.T., Fortulan, C.A., Bonagamba, T.J., 2016. T 2 -Filtered T 2 − T 2 Exchange NMR. J Chem Phys 144, 204201. https://doi.org/10.1063/1.4951712

El Husseiny, A., Vanorio, T., 2015. The effect of micrite content on the acoustic velocity of carbonate rocks. GEOPHYSICS 80, L45–L55. https://doi.org/10.1190/geo2014-0599.1

Elsayed, H., Picicco, M., Ferroni, L., Gardin, C., Zavan, B., Bernardo, E., 2020. Novel bioceramics from digital light processing of calcite/acrylate blends and low temperature pyrolysis. Ceram Int 46, 17140–17145. https://doi.org/10.1016/j.ceramint.2020.03.277

Escardino, A., García-Ten, J., Feliu, C., Saburit, A., Cantavella, V., 2013. Kinetic study of the thermal decomposition process of calcite particles in air and CO2 atmosphere. Journal of Industrial and Engineering Chemistry 19, 886–897. https://doi.org/10.1016/j.jiec.2012.11.004

Fahim Salek, M., Shinde, V. V, Beckingham, B.S., Beckingham, L.E., 2022. Resin based 3D printing for fabricating reactive porous media. Mater Lett 322, 132469. https://doi.org/10.1016/j.matlet.2022.132469

Fedrizzi, R.M., Ceia, M.A.R. de, Misságia, R.M., Santos, V.H., Lima Neto, I., 2018. Artificial carbonate rocks: Synthesis and petrophysical characterization. J Pet Sci Eng 163, 303–310. https://doi.org/10.1016/j.petrol.2017.12.089

Ferrari, J.V., Silveira, B.M. de O., Arismendi-Florez, J.J., Fagundes, T.B., Silva, M.A. da T., Skinner, R., Ulsen, C., Carneiro, C. de C., 2021. Influence of carbonate reservoir mineral heterogeneities on contact angle measurements. J Pet Sci Eng 199, 108313. https://doi.org/10.1016/j.petrol.2020.108313

Florez, J.J.A., Ferrari, J.V., 2021. Preliminary analyses of synthetic carbonate plugs: consolidation, petrophysical and wettability properties. Oil & Gas Science and Technology – Revue d'IFP Energies nouvelles 76, 12. https://doi.org/10.2516/ogst/2020087

Florez, J.J.A., Ferrari, J.V., Michelon, M., Ulsen, C., 2019. Construction of synthetic carbonate plugs: A review and some recent developments. Oil & Gas Science and Technology – Revue d'IFP Energies nouvelles 74. https://doi.org/10.2516/ogst/2019001

Fu, J.Y., Yue, X., Zhang, B., 2020. Methodology for Concurrent Multi-Parametric Physical Modeling of a Target Natural Unfractured Homogeneous Sandstone. Processes 8, 1448. https://doi.org/10.3390/pr8111448

Ganat, T.A.-A.O., 2020. Fundamentals of Reservoir Rock Properties, Fundamentals of Reservoir Rock Properties. Springer International Publishing, Cham. https://doi.org/10.1007/978-3-030-28140-3

Gell, E.M., Walley, S.M., Braithwaite, C.H., 2019. Review of the Validity of the Use of Artificial Specimens for Characterizing the Mechanical Properties of Rocks. Rock Mech Rock Eng 52, 2949–2961. https://doi.org/10.1007/s00603-019-01787-8

Gibson, I., Rosen, D., Stucker, B., 2015. Additive manufacturing technologies: 3D printing, rapid prototyping, and direct digital manufacturing, second edition, 2nd ed, Additive Manufacturing Technologies: 3D Printing, Rapid Prototyping, and Direct Digital Manufacturing, Second Edition. Springer New York, New York, NY. https://doi.org/10.1007/978-1-4939-2113-3

Head, D., Vanorio, T., 2016. Effects of changes in rock microstructures on permeability: 3-D printing investigation. Geophys Res Lett 43, 7494–7502. https://doi.org/10.1002/2016GL069334

Heap, M., Reuschlé, T., Baud, P., Renard, F., Iezzi, G., 2018. The permeability of stylolite-bearing limestone. J Struct Geol 116, 81–93. https://doi.org/10.1016/j.jsg.2018.08.007

Ishutov, S., 2019. Establishing Framework for 3D Printing Porous Rock Models in Curable Resins. Transp Porous Media 129, 431–448. https://doi.org/10.1007/s11242-019-01297-9

Ishutov, S., Hasiuk, F.J., Fullmer, S.M., Buono, A.S., Gray, J.N., Harding, C., 2017. Resurrection of a reservoir sandstone from tomographic data using three-dimensional printing. Am Assoc Pet Geol Bull 101, 1425–1443. https://doi.org/10.1306/11111616038

Ishutov, S., Hasiuk, F.J., Jobe, D., Agar, S., 2018a. Using Resin-Based 3D Printing to Build Geometrically Accurate Proxies of Porous Sedimentary Rocks. Groundwater 56, 482–490. https://doi.org/10.1111/gwat.12601

Ishutov, S., Jobe, T.D., Zhang, S., Gonzalez, M., Agar, S.M., Hasiuk, F.J., Watson, F., Geiger, S., Mackay, E., Chalaturnyk, R., 2018b. Three-dimensional printing for geoscience: Fundamental research, education, and applications for the petroleum industry. Am Assoc Pet Geol Bull 102, 1–26. https://doi.org/10.1306/0329171621117056

Ji, Y., Baud, P., Vajdova, V., Wong, T. -f., 2012. Characterization of Pore Geometry of Indiana Limestone in Relation to Mechanical Compaction. Oil & Gas Science and Technology – Revue d'IFP Energies nouvelles 67, 753–775. https://doi.org/10.2516/ogst/2012051

Ji, Y., Hall, S.A., Baud, P., Wong, T., 2015. Characterization of pore structure and strain localization in Majella limestone by X-ray computed tomography and digital image correlation. Geophys J Int 200, 701–719. https://doi.org/10.1093/gji/ggu414

Kong, L., 2019. Innovation of Petrophysical and Geomechanical Experiment Methodologies: the Application of 3D Printing Technology. University of North Dakota.

Kong, L., Ishutov, S., Hasiuk, F., Xu, C., 2021a. 3D Printing for Experiments in Petrophysics, Rock Physics, and Rock Mechanics: A Review. SPE Reservoir Evaluation & Engineering 24, 721–732. https://doi.org/10.2118/206744-pa

Kong, L., Ostadhassan, M., Hou, X., Mann, M., Li, C., 2019a. Microstructure characteristics and fractal analysis of 3D-printed sandstone using micro-CT and SEM-EDS. J Pet Sci Eng 175, 1039–1048. https://doi.org/10.1016/j.petrol.2019.01.050

Kong, L., Ostadhassan, M., Liu, B., Eshraghi, M., Li, C., Navarro, M., Zhang, Y., Wei, H., 2021b. A comparison of three-dimensional–printed porous rocks with nano x-ray computed tomography: Silica sand, gypsum powder, and resin. Am Assoc Pet Geol Bull 105, 2245–2261. https://doi.org/10.1306/08142019028

Kong, L., Ostadhassan, M., Liu, B., Li, C., Liu, K., 2019b. Multifractal Characteristics of MIP-Based Pore Size Distribution of 3D-Printed Powder-Based Rocks: A Study of Post-Processing Effect. Transp Porous Media 129, 599–618. https://doi.org/10.1007/s11242-018-1152-9

Kushnir, A.R.L., Kennedy, L.A., Misra, S., Benson, P., White, J.C., 2015. The mechanical and microstructural behaviour of calcite-dolomite composites: An experimental investigation. J Struct Geol 70, 200–216. https://doi.org/10.1016/j.jsg.2014.12.006

Ladd, M., Palmer, R., 2013. Powder Diffraction, in: Structure Determination by X-Ray Crystallography. Springer US, Boston, MA, pp. 585–634. https://doi.org/10.1007/978-1-4614-3954-7_12

Leoni, M., 2019. X-Ray Powder Diffraction, in: Materials Characterization, Vol 10, ASM Handbook. ASM International, pp. 399–413. https://doi.org/10.31399/asm.hb.v10.a0006680

Lézin, C., Odonne, F., Massonnat, G.J., Escadeillas, G., 2009. Dependence of joint spacing on rock properties in carbonate strata. Am Assoc Pet Geol Bull 93, 271–290. https://doi.org/10.1306/09150808023

Lin, P.W., Shen, P., 2013. Onset sintering-coarsening-coalescence kinetics of calcite powders. J Eur Ceram Soc 33, 3265–3272. https://doi.org/10.1016/j.jeurceramsoc.2013.06.023

Loucks, R.G., Reed, R.M., Ruppel, S.C., Hammes, U., 2012. Spectrum of pore types and networks in mudrocks and a descriptive classification for matrix-related mudrock pores. Am Assoc Pet Geol Bull 96, 1071–1098. https://doi.org/10.1306/08171111061

Lucas, C.R. dos S., Aum, Y.K.P.G., Araújo, E. de A., Castro Dantas, T.N. de, Araújo, E.A., Sousa, T.N., Aum, P.T.P., 2020. Investigating the Fluid–Solid Interaction of Acid Nonionic Nanoemulsion with Carbonate Porous Media. Molecules 25, 1475. https://doi.org/10.3390/molecules25061475

Lucas-Oliveira, E., Araujo-Ferreira, A.G., Trevizan, W.A., Coutinho dos Santos, B.C., Bonagamba, T.J., 2020. Sandstone surface relaxivity determined by NMR T2 distribution and digital rock simulation for permeability evaluation. J Pet Sci Eng 193, 107400. https://doi.org/10.1016/j.petrol.2020.107400

Lucas-Oliveira, E., Araujo-Ferreira, A.G., Trevizan, W.A., Fortulan, C.A., Bonagamba, T.J., 2018. Computational approach to integrate 3D X-ray microtomography and NMR data. Journal of Magnetic Resonance 292, 16–24. https://doi.org/10.1016/j.jmr.2018.05.001

Machel, H.G., 2005. SEDIMENTARY ROCKS | Dolomites, in: Encyclopedia of Geology. Elsevier, pp. 79–94. https://doi.org/10.1016/B0-12-369396-9/00308-7

Meiboom, S., Gill, D., 2004. Modified Spin-Echo Method for Measuring Nuclear Relaxation Times. Review of Scientific Instruments 29, 688. https://doi.org/10.1063/1.1716296

Monchau, F., Hivart, P., Genestie, B., Chai, F., Descamps, M., Hildebrand, H.F., 2013. Calcite as a bone substitute. Comparison with hydroxyapatite and tricalcium phosphate with regard to the osteoblastic activity. Materials Science and Engineering C 33, 490–498. https://doi.org/10.1016/j.msec.2012.09.019

Morais, M.M., Camargo, I.L. de, Colombo, P., Fortulan, C.A., 2023. Additive manufacturing of calcium carbonate parts through vat-photopolymerization and sintering in carbon dioxide atmosphere. Open Ceramics 14, 100348. https://doi.org/10.1016/j.oceram.2023.100348

Morais, M.M., Salomão, R.D., Fortulan, C.A., 2022. Successful and failed attempts to obtain bulk calcium carbonate parts through sintering and carbonation, in: Proceedings of the 65º-66º Congresso Brasileiro de Cerâmica. Associação Brasileira de Cerâmica, Águas de Lindóia, SP.

Olszak-Humienik, M., Jablonski, M., 2015. Thermal behavior of natural dolomite. J Therm Anal Calorim 119, 2239–2248. https://doi.org/10.1007/s10973-014-4301-6

Piane, Delle, C., Clennell, M.B., Dautriat, J., Price, G., 2015. Fluid/Rock Interactions in Porous Carbonate Rocks: An Integrated Mechanical, Ultrasonic and Micro-Structural Study, in: AAPG International Conference and Exhibition, Melbourne, Australia 13-16 September 2015. Society of Exploration Geophysicists and American Association of Petroleum Geologists, pp. 204–204. https://doi.org/10.1190/ice2015-2210005

Putri, T.S., Hayashi, K., Ishikawa, K., 2020. Fabrication of three-dimensional interconnected porous blocks composed of robust carbonate apatite frameworks. Ceram Int 46, 20045–20049. https://doi.org/10.1016/j.ceramint.2020.05.076

Reed, J.S., 1995. Principles of ceramics processing, 2nd ed. ed. John Wiley & Sons, New York.

Regnet, J.B., Robion, P., David, C., Fortin, J., Brigaud, B., Yven, B., 2015. Acoustic and reservoir properties of microporous carbonate rocks: Implication of micrite particle size and morphology. J Geophys Res Solid Earth 120, 790–811. https://doi.org/10.1002/2014JB011313

Richerson, D.W., Lee, W.E., 2018. Modern Ceramic Engineering, 4th ed. CRC Press. https://doi.org/10.1201/9780429488245

Sammis, C.G., Ashby, M.F., 1986. The failure of brittle porous solids under compressive stress states. Acta Metallurgica 34, 511–526. https://doi.org/10.1016/0001-6160(86)90087-8

Sauerwein, M., Doubrovski, E.L., 2018. Local and recyclable materials for additive manufacturing: 3D printing with mussel shells. Mater Today Commun 15, 214–217. https://doi.org/10.1016/j.mtcomm.2018.02.028

Schön, J.H., 2011. Chapter 2 - Pore Space Properties, in: Physical Properties of Rocks. Elsevier, pp. 17–73. https://doi.org/10.1016/S1567-8032(11)08002-5

Selley, R. C., 2005. SEDIMENTARY ROCKS/Mineralogy and Classification, in: Encyclopedia of Geology. pp. 25–37. https://doi.org/https://doi.org/10.1016/B0-12-369396-9/00304-X

Selley, R C, 2005. SEDIMENTARY ROCKS/Limestones, in: Encyclopedia of Geology. pp. 107–113. https://doi.org/https://doi.org/10.1016/B0-12-369396-9/00305-1

Shaked, H., Polishchuk, I., Nagel, A., Bekenstein, Y., Pokroy, B., 2021. Long-term stabilized amorphous calcium carbonate—an ink for bio-inspired 3D printing. Mater Today Bio 11, 100120. https://doi.org/10.1016/j.mtbio.2021.100120

Someya, N., Kitazato, T., Fujikawa, T., Manabe, Y., 1993. SINTERED BODY OF CALCIUM CARBONATE AND PROCESS FOR PRODUCING SAME. Patent US 5187125A.

Speight, J.G., 2017. Reservoirs and Reservoir Fluids, in: Deep Shale Oil and Gas. Elsevier, pp. 63–120. https://doi.org/10.1016/B978-0-12-803097-4.00002-4

Stern, K.H., Weise, E.L., 1969. High Temperature Properties and Decomposition of Inorganic Salts. Part 2. Carbonates. NATIONAL STANDARD REFERENCE DATA SYSTEM.

Studart, A.R., Gonzenbach, U.T., Tervoort, E., Gauckler, L.J., 2006. Processing routes to macroporous ceramics: A review. Journal of the American Ceramic Society 89, 1771–1789. https://doi.org/10.1111/j.1551-2916.2006.01044.x

Subagjo, Wulandari, W., Adinata, P.M., Fajrin, A., 2017. Thermal decomposition of dolomite under CO2-air atmosphere. p. 040006. https://doi.org/10.1063/1.4974427

Tarì, G., Ferreira, J.M.F., 1998. Colloidal Processing of Calcium Carbonate. Ceram Int 24, 527–532. https://doi.org/10.1016/S0272-8842(97)00052-7

Tikhonova, S.A., Evdokimov, P. V., Prosvirnin, D. V., Novoseletskaya, E.S., Efimenko, A.Y., Putlyaev, V.I., 2021. Fabrication of Calcium Phosphate Bioceramics with a Uniform Distribution of Pores of a Given Size. Russian Metallurgy (Metally) 2021, 381–385. https://doi.org/10.1134/S0036029521040339

Tucker, M.E., Wright, V.P., 1990. Carbonate Sedimentology. Blackwell Publishing Ltd., Oxford, UK. https://doi.org/10.1002/9781444314175

Valverde, J.M., Sanchez-Jimenez, P.E., Perez-Maqueda, L.A., 2015. Limestone Calcination Nearby Equilibrium: Kinetics, CaO Crystal Structure, Sintering and Reactivity. The Journal of Physical Chemistry C 119, 1623–1641. https://doi.org/10.1021/jp508745u

Van Stappen, J.F., De Kock, T., De Schutter, G., Cnudde, V., 2019. Uniaxial compressive strength measurements of limestone plugs and cores: a size comparison and X-ray CT study. Bulletin of Engineering Geology and the Environment 78, 5301–5310. https://doi.org/10.1007/s10064-018-01448-0

Viswanathan, R., Narasimhan, T.S.L., Nalini, S., 2010. Study of incongruent decomposition of calcium carbonate by transpiration thermogravimetry. J Chem Eng Data 55, 3779–3785. https://doi.org/10.1021/je100294t

Wang, Z., Wang, R., Li, T., Zhao, M., 2017. The combined effects of pore structure and pore fluid on the acoustic properties of cracked and vuggy synthetic rocks. J Pet Sci Eng 156, 202–211. https://doi.org/10.1016/j.petrol.2017.05.023

Wang, Z., Wang, R., Wang, F., Qiu, H., Li, T., 2015. Experiment study of pore structure effects on velocities in synthetic carbonate rocks. GEOPHYSICS 80, D207–D219. https://doi.org/10.1190/geo2014-0366.1

Wu, H., Papazoglou, A., Viggiani, G., Dano, C., Zhao, J., 2020. Compaction bands in Tuffeau de Maastricht: insights from X-ray tomography and multiscale modeling. Acta Geotech 15, 39–55. https://doi.org/10.1007/s11440-019-00904-9

Yasar, E., Erdogan, Y., 2004. Correlating sound velocity with the density, compressive strength and Young's modulus of carbonate rocks. International Journal of Rock Mechanics and Mining Sciences 41, 871–875. https://doi.org/10.1016/j.ijrmms.2004.01.012

Zakaria, A.S., Nasr-El-Din, H.A., Ziauddin, M., 2015. Flow of emulsified acid in carbonate rocks. Ind Eng Chem Res 54, 4190–4202. https://doi.org/10.1021/ie504167y

Zhu, W., Baud, P., Wong, T., 2010. Micromechanics of cataclastic pore collapse in limestone. J Geophys Res 115, B04405. https://doi.org/10.1029/2009JB006610